



Charge-4e supercurrent in a two-dimensional InAs-Al superconductor-semiconductor heterostructure

Carlo Ciaccia¹, Roy Haller¹, Asbjørn C. C. Drachmann^{2,3}, Tyler Lindemann^{4,5}, Michael J. Manfra^{4,5,6,7}, Constantin Schrade^{2,8} & Christian Schönenberger^{1,9}

Superconducting qubits with intrinsic noise protection offer a promising approach to improve the coherence of quantum information. Crucial to such protected qubits is the encoding of the logical quantum states into wavefunctions with disjoint support. Such encoding can be achieved by a Josephson element with an unusual charge-4e supercurrent emerging from the coherent transfer of pairs of Cooper-pairs. In this work, we demonstrate the controlled conversion of a conventional charge-2e dominated to a charge-4e dominated supercurrent in a superconducting quantum interference device (SQUID) consisting of gate-tunable planar Josephson junctions. We investigate the ac Josephson effect of the SQUID and measure a dominant photon emission at twice the fundamental Josephson frequency together with a doubling of the number of Shapiro steps, both consistent with the appearance of charge-4e supercurrent. Our results present a step towards protected superconducting qubits based on superconductor-semiconductor hybrid materials.

¹Quantum- and Nanoelectronics Lab, University of Basel, 4056 Basel, Switzerland. ²Center for Quantum Devices, Niels Bohr Institute, University of Copenhagen, 2100 Copenhagen, Denmark. ³NNF Quantum Computing Programme, Niels Bohr Institute, University of Copenhagen, 2100 Copenhagen, Denmark. ⁴Department of Physics and Astronomy, Purdue University, West Lafayette, IN 47907, USA. ⁵Birck Nanotechnology Center, Purdue University, West Lafayette, IN 47907, USA. ⁶School of Electrical and Computer Engineering, Purdue University, West Lafayette, IN 47907, USA. ⁷School of Materials Engineering, Purdue University, West Lafayette, IN 47907, USA. ⁸Hearne Institute for Theoretical Physics, Department of Physics and Astronomy, Louisiana State University, Baton Rouge, LA 70803, USA. ⁹Swiss Nanoscience Institute, University of Basel, Klingelbergstrasse 82, Basel, Switzerland. ✉email: Carlo.Ciaccia@unibas.ch

The Josephson effect describes the dissipationless current flow between two weakly coupled superconductors. Today, numerous technologies are based on this fundamental quantum phenomenon, ranging from superconducting qubit devices^{1–5} to parametric amplifiers^{6–8}.

Regardless of whether the weak link consists of an insulator or a normal conducting material, the supercurrent is a periodic function of the phase difference φ between the superconductors⁹. In a Josephson tunnel junction, the supercurrent arises from the coherent tunneling of individual Cooper-pairs through the insulating barrier, each carrying a charge $2e$ ¹⁰. The current-phase relation (CPR) in this case is given by $I(\varphi) = I_c \sin(\varphi)$, with I_c being the critical current. However, when the superconductors are separated by a conducting weak link, such as a semiconductor or a metal, coherent transport of multiple Cooper-pairs can also occur, resulting in a non-sinusoidal CPR^{11–15}. In general, the CPR of the junction can be expanded in a Fourier series as:

$$I(\varphi) = \sum_{m=1}^{\infty} c_m \sin(m\varphi). \quad (1)$$

The $\sin(m\varphi)$ terms correspond to processes involving the simultaneous, coherent transport of m Cooper-pairs carrying a charge $m \times 2e$. The amplitude of the higher harmonic terms c_m , $m > 1$, reflects the probability of multi-Cooper-pair transport and decreases with higher harmonics, indicating that transport across the junction arises mainly from individual Cooper-pairs. Often, the CPR can be described by the junction transparency τ , defined as the transmission probability of electron in the weak link. The more transparent a junction is, the higher the ratio between successive Fourier coefficients $|c_{m+1}(\tau)/c_m(\tau)|$.

Several theoretical proposals^{16–24} have investigated the possible advantages of using a so-called $\sin(2\varphi)$ Josephson junction (JJ) for the realization of a parity-protected superconducting qubit. In this case, the parity of the Cooper pairs is protected by using a Josephson element with a dominant second harmonic term c_2 in Eq. (1), corresponding to the supercurrent being carried by pairs of Cooper pairs with charge $4e$. The qubit states can be therefore encoded into the even and odd parity of the number of Cooper-pairs on a superconducting island.

Important steps towards realizing a parity-protected qubit have been taken with superconducting quantum interference devices (SQUIDs) made of tunnel junctions arranged in a rhombus geometry^{25,26}. By designing the loop inductances and the junction's position, it is possible to engineer a CPR with a large second harmonic component $|c_2/c_1| \sim 0.5$ ²⁷, corresponding to an effective transparency $\tau^* \sim 1$ ^{28,29}. When the magnetic flux through the SQUID is tuned to half a flux quantum $\Phi_0/2$, the first harmonic is suppressed due to destructive interference, leaving a dominant second harmonic term. This method relies on the fabrication of identical junctions, and departures from symmetry spoils parity protection.

A promising alternative approach is based on gate-tunable hybrid superconducting-semiconducting materials with high transparency channels. In ref. ³⁰ the authors realize a $\sin(2\varphi)$ element with a SQUID made of proximitized InAs nanowires, where local gate control of each junction allows precise balancing of the first harmonics. They show that the qubit relaxation time increases by an order of magnitude when the qubit is tuned close to the protected regime. However, for practical use of the parity-protected qubit, the Josephson energy of the second harmonics in the balanced configuration must be at the same time much larger than the residual Josephson energy coming from the first harmonics (for a long relaxation time) and much larger than the island charging energy (for small dephasing rate). The few conduction channels in the nanowires limit the maximum obtainable critical current and make the last requirement difficult to satisfy.

Hybrid two-dimensional materials have seen in recent years a great improvement in growth techniques that allow up-scaling and offer the advantage of wide gate tunability and top-down fabrication^{31,32}. In this work, we report the observation of a 4e supercurrent in a SQUID consisting of two planar Josephson junctions formed in an InAs two-dimensional electron gas proximitized by an epitaxial Al layer^{33,34}. Even if the operation of superconducting qubits has already been shown in this material platform³⁵, the realization of high-quality resonators on III-V substrates remains a challenging task. Therefore, here we investigate the contribution of the 4e supercurrent by measuring the evolution in frequency of the ac Josephson radiation emitted by the SQUID as a function of a dc bias voltage. The high transparency of these JJs¹³ allows us to engineer an effective CPR in which the first harmonic is suppressed due to destructive interference, leaving a dominant second harmonic term. To achieve this, we balance the critical current of the junctions with local gate voltages and tune the magnetic flux through the SQUID loop to half a flux quantum $\Phi_0/2$. In the balanced configuration, radiation measurements reveal a pronounced suppression of emission at the fundamental Josephson frequency in favor of a strong ac signal at twice this frequency. We corroborate this finding by additionally detecting fractional half-Shapiro steps, characteristic of a $\sin(2\varphi)$ junction.

Results and Discussion

Device and procedures. A simplified schematic of the device is shown in Fig. 1a. A superconducting loop, threaded by an external magnetic flux Φ_{ext} , is interrupted on each arm by a section where the superconductor has been selectively removed. The Josephson junctions are formed in an InAs two-dimensional electron gas (green) which is proximitized by the close vicinity to an epitaxial Al layer (blue) grown on top. By locally removing the Al top layer with etching techniques that are detailed in the Methods section, we form InAs weak links. Local gate electrodes, V_{G1} and V_{G2} , allow us to tune the electron density in the weak links and, consequently, adjust the critical currents of the JJs. The hereby formed Josephson junctions are symmetric by design, but the wet etching step produced two different widths: $\sim 3 \mu\text{m}$ for JJ_1 and $\sim 2.5 \mu\text{m}$ for JJ_2 . Despite fabrication-related asymmetries, we were still able to tune the SQUID into a symmetric configuration by leveraging the gate tunability of the semiconducting weak link. Junctions this wide typically contain many conduction channels with a bimodal distribution of transparency values distributed between zero and one^{36–39}. Earlier experiments on the same material platform have shown that the CPR in these junctions can be described by a single channel short diffusive junction model^{13,40} with an effective transparency $\tau^* \sim 0.86$.

Figure 1b depicts a false-color electron micrograph of the device and the experimental setup. We apply a dc-current via the voltage drop over a bias resistor $R_b = 1 \text{ M}\Omega$. We damp the SQUID with a shunt resistor $R_s = 10 \Omega$ to enable a continuous transition from the superconducting to the normal conducting state. The 10Ω -shunt increases the region of the stable voltage drop across the junction, and at the same time, it reduces both heating and hysteretic behaviors. The differential resistance is measured using standard lock-in techniques. Furthermore, the microwave setup allows probing the ac Josephson effect in two ways. On one hand, the Josephson radiation emitted from the SQUID under finite dc bias can be detected with a spectrum analyzer. Second, the reverse experiment can be performed, namely, irradiating the device with a microwave tone and measuring its dc response.

Figure 1c shows the interference between the supercurrent I_1 flowing in JJ_1 (blue dashed curve) and the supercurrent I_2 in JJ_2

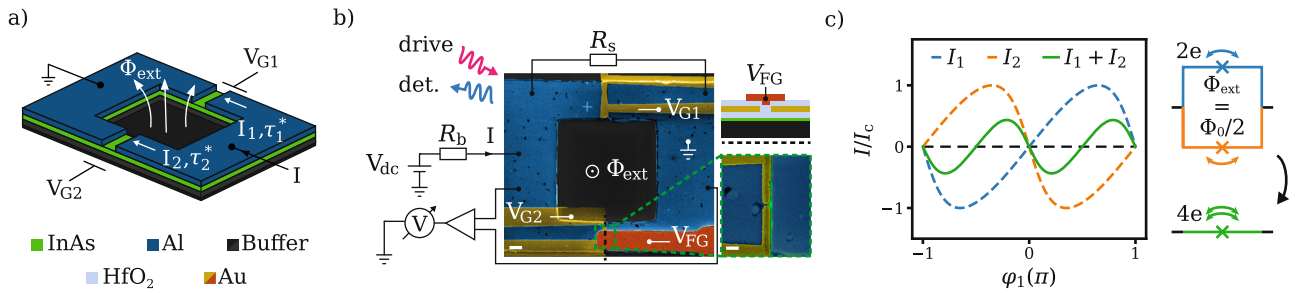


Fig. 1 Device description and measurement setup. **a** Circuit schematic of a dc superconducting quantum interference device (SQUID) formed by two gate-tunable Josephson junctions with effective transmission probabilities τ_1^* , τ_2^* , threaded by the external flux Φ_{ext} . **b** False-color electron micrograph of the device and experimental setup. Each junction is fabricated by selectively removing the epi-Al layer (blue) over 150 nm long stripes. The charge carrier density in the exposed InAs two-dimensional electron gas (green) is tuned by a set of electrostatic gates (V_{G1} , V_{G2} , and V_{FG}) shown in yellow and orange, which are galvanically isolated from the loop by 15 nm of HfO_2 (light blue). dc and ac current bias is defined through the voltage drop over a bias resistor $R_b = 1 \text{ M}\Omega$. The SQUID is shunted to the ground with $R_s = 10 \Omega$. We send a microwave tone to the device and also detect photon emission. The scale bar in the main figure is $1 \mu\text{m}$, and the scale bar in the zoom-in is 300 nm . **c** Individual components I_1 (blue) and I_2 (orange) and total current (green) flowing through a symmetric SQUID as a function of the phase drop φ_1 at $\Phi_{\text{ext}} = \Phi_0/2$. The current phase relation of both junctions is plotted using a single channel short diffusive model with an effective transparency $\tau^* = 0.86$. The current is normalized to units of the critical current I_c . The schematic of the SQUID helps visualize the requirements for a $\sin(2\varphi)$ junction: a dominant $4e$ supercurrent is obtained with a symmetric SQUID biased at $\Phi_0/2$.

(orange dashed curve) at $\Phi_{\text{ext}} = \Phi_0/2$. The total supercurrent flowing through the SQUID (green solid curve) is:

$$I = I_1(\varphi_1, \tau_1^*) + I_2(\varphi_2, \tau_2^*). \quad (2)$$

The phase drops over the two JJs are related by the fluxoid relation $\varphi_1 - \varphi_2 = 2\pi\Phi_{\text{ext}}/\Phi_0$. Here, we have assumed that the phase difference between the two JJs is solely given by the externally applied flux, neglecting loop, and mutual inductances, which is justified in our device⁴⁰. When the loop is flux biased at $\Phi_{\text{ext}} = \Phi_0/2$ and the JJs are the same ($\tau_1^* = \tau_2^*$), Cooper-pairs are transferred with the same amplitude but opposite phase through the SQUID arms, resulting in a destructive interference of the $2e$ contribution with periodicity 2π and in a constructive interference of the $4e$ supercurrent with periodicity π . In this way, it is possible to engineer an effective $\sin(2\varphi)$ junction.

ac and dc Josephson effect from single junction. In the following, we characterize the dc and ac Josephson effect of the individual JJs. To this end, we measure the gate dependence of the critical current and the radiation spectrum of each junction, while the neighboring one is fully depleted. Figure 2a, b show the differential resistance of JJ_1 and JJ_2 as a function of current bias I for different gate voltages. We identify the critical current I_c as the boundary between the superconducting regime (dark blue) and the ohmic regime (turquoise). At negative gate voltages ($V_{G1} \leq -0.9 \text{ V}$ and $V_{G2} \leq -1.5 \text{ V}$) I_c is negligibly small, but it can be gradually increased with increasing V_{Gi} . $I_{c,\text{max}}$ saturates to $I_{c1,\text{max}} = 1.1 \mu\text{A}$ for JJ_1 and $I_{c1,\text{max}} = 0.8 \mu\text{A}$ for JJ_2 at around $V_{Gi} = 0.5 \text{ V}$. The slight differences in the gate dependence of the two junctions are attributed to a different junction width and gate geometry. To estimate the $I_c R_n$ product of the junctions, we measure the resistance at voltage bias larger than twice the superconducting gap of the leads as obtained from multiple Andreev reflection measurements conducted on a different chip of the same wafer. Subtracting the shunt resistor, we obtain a normal state resistance of the junction $R_n \sim 90 \Omega$, corresponding to a $I_c R_n \sim 90 \mu\text{V}$. We also note that potential errors in estimating R_n might have led to an underestimation of the $I_c R_n$ product. Nonetheless, the significantly large $I_c R_n$ product indicates a high-quality Josephson junction with a uniform current distribution.

In Fig. 2c, d, the IV -curves at $V_{G1} = -0.75 \text{ V}$ and $V_{G2} = -0.7 \text{ V}$, respectively are obtained by integrating the measured dV/dI curves along the white dashed lines in Fig. 2a, b. Both junctions show an

ohmic behavior down to $2 \mu\text{V}$, which allows stable voltage biasing in the microwave regime of the Josephson emission.

According to the ac Josephson effect, the phase difference of a voltage-biased Josephson junction will evolve linearly in time following

$$\varphi(t) = \frac{2\pi}{\Phi_0} Vt, \quad (3)$$

with V being the voltage drop across the junction. Consequently, an applied dc voltage causes an oscillating supercurrent at the Josephson frequency $f_j = 2eV/h$. This transforms into the emission of microwave photons at f_j . If higher harmonics are present, photon emission at higher frequencies $f_{j,m} = m \times 2eV/h$ also occurs^{41,42}. In Fig. 2e we show the expected peak evolution in the emission spectrum of voltage-biased JJ as a function of detection frequency f_{det} and V . For every voltage bias position, peaks emerge in the emission spectrum, if the detection frequency matches an integer multiple of the Josephson frequency $f_{\text{det}} = f_{j,m}$. These peaks induce a fan-like pattern, capturing the linear relation between voltage and the emission frequency with slope $h/(m2e)$. Emission lines evolving as $hf_{\text{det}}/(m2e)$ correspond to the coherent transport of m Cooper-pairs across the junction (red, orange, and pink dashed lines for $m = 1, 2$, and 3). In addition to the fan-like pattern, replicas of the Josephson emission lines can appear at a constant frequency offset on the right and on the left of the predicted peak position due to photon-assisted emission through environmental modes⁴³. A photon from a spurious environmental mode can be upconverted to a detector photon by taking up the energy $2eV$ provided by the inelastic tunneling of a Cooper-pair (right shift in frequency). The energy balance in this case reads $hf_{\text{det}} = hf_{\text{env}} + 2eV$, where f_{env} corresponds to the resonant frequency of an environmental cavity. Such resonance can be caused for example by a standing wave pattern along the microwave lines. The complementary process is also possible, meaning that a photon coming from a Cooper-pair tunneling can be downconverted to a detector photon by giving up the energy hf_{env} to the environment (left shift in frequency). The energy balance in this case reads $hf_{\text{det}} = 2eV - hf_{\text{env}}$.

In Fig. 2f, g we plot the normalized radiation power $P_{\text{det, norm}}$ as a function of f_{det} and V_{int} for JJ_1 and JJ_2 respectively. The power is normalized at each detection frequency to compensate for the frequency-dependent background. A pronounced emission peak at frequency $f_{j,1}$ (red dashed line) corresponding to the $2e$ single

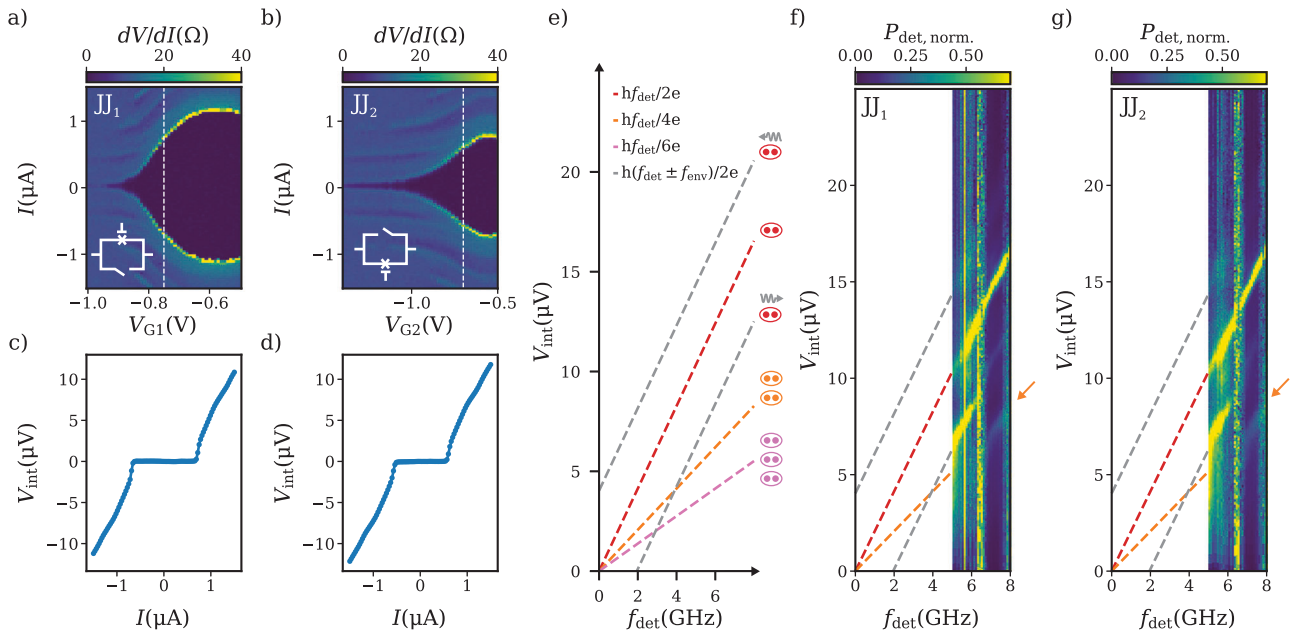


Fig. 2 dc and ac Josephson effect of the individual junctions. **a, b** Differential resistance dV/dI of the individual Josephson junctions JJ_1 and JJ_2 as a function of gate voltage V_{G1} , V_{G2} and current bias I . **c, d** Integrated voltage V_{int} as a function of current bias I at $V_{G1} = -0.75$ V and $V_{G2} = -0.7$ V obtained by integrating the corresponding dV/dI along the white dashed lines shown in **a, b**. **e** Illustration of the expected peak evolution in the emission spectrum of voltage-biased JJ as a function of detection frequency f_{det} . A junction with finite transparency emits photons at the fundamental Josephson frequency (red dashed line) and integer multiples of it (orange and pink dashed lines), here corresponding to the coherent transport of pairs of Cooper-pairs. The dashed gray lines indicate processes associated with the up- and down-conversion of environmental photons at frequency f_{env} . **f, g** Normalized radiation power $P_{det, norm.}$ as a function of f_{det} and V_{int} for the same configuration in **c** and **d**. The orange arrow points to the $4e$ emission peak.

Cooper-pair transport is measured over the entire frequency range from 5 GHz to 8 GHz. The signal due to the $4e$ double Cooper-pair transport at frequency $f_{J,2}$ (orange dashed line) is weaker but becomes clearly visible in the emission spectrum around 7 GHz (orange arrow). Emission peaks at frequencies corresponding to higher harmonics, $m > 2$, are below our detection limit. In addition to the fan-like pattern, there is a strong replica of the fundamental Josephson emission appearing at a constant frequency offset ($f_{env} \sim 1.95$ GHz) on the right of the predicted peak position. Its contribution diminishes for $f_{det} > 6$ GHz. Changes in power spectrum as a function of detection frequency arise from a frequency-dependent probability of photon emission due to inelastic Cooper pair tunneling. The emission probability depends on the impedance of the environment surrounding the Josephson junction⁴⁴, which in turn has a complex behavior as a function of frequency caused, for example, by standing wave patterns in the rf lines due to spurious impedance mismatch conditions. By setting $f_{det} = 7.1$ GHz, we can disregard the contribution of this environmental mode in the following investigation.

ac and dc Josephson effect from a SQUID. Next, we exploit the interference between the two junctions when both carry a finite supercurrent in order to realize an effective Josephson element with the negligible first harmonic component. We require two conditions: (i) the flux is to be set to $\Phi_{ext} = \Phi_0/2$, and (ii), the JJs are gate-tuned into balance, such that $c_{1,JJ_1} = c_{1,JJ_2}$. The key challenge in the experiment is the balancing of the junctions. As a solution, we adopt an approach proposed in⁴⁵ that is based on the observation that I_c for the forward and reverse current-bias directions, $I_{c,+}$ and $I_{c,-}$, is mismatched unless both junctions are balanced and $\Phi_{ext} = n\Phi_0/2$ with n being an integer. To balance the SQUID, we look at regions in gate voltage without diode effect, meaning $I_{c,+}$ and $I_{c,-}$ are equal (symmetric junctions).

In Fig. 3 we measure the SQUID in three different configurations. Firstly, we fix the gate voltages such that the junctions are symmetric and sweep Φ_{ext} . Secondly, we fix V_{G2} and sweep V_{G1} at $\Phi_{ext} = \Phi_0/2$. Finally, we fix the gate voltages and sweep Φ_{ext} in the case of asymmetric junctions.

In Fig. 3a we plot the SQUID differential resistance dV/dI as a function of current bias I and Φ_{ext} in a gate configuration where $I_{c1} \approx I_{c2}$. No diode effect is observed over the entire flux bias range. Differences between the gate values at which symmetry is achieved and those expected from Fig. 2a, b are caused by the fact that the critical current of each junction depends on whether the junction is measured individually or embedded in SQUID⁴⁶. Simultaneously, we measure the SQUID ac emission at fixed detection frequency $f_{det} = 7.1$ GHz. Figure 3b shows the normalized radiation power $P_{det, norm.}$ as a function of Φ_{ext} and integrated voltage drop over the SQUID V_{int} . Because the signal peaks at $V_m = hf_{det}/(m2e)$, we scale the voltage axis by $hf_{det}/2e$. The emission pattern changes in a striking manner around $\Phi_{ext} = \Phi_0/2$. The fundamental Josephson signal at a scaled $V_{int} = 1$, corresponding to the $2e$ supercurrent, vanishes almost completely, while a sharp bright peak at a scaled $V_{int} = 1/2$ appears, which corresponds to the radiation signal coming from the simultaneous inelastic transport of pairs of Cooper-pairs. An additional horizontal line is visible in the map due to the spurious environmental mode, as addressed before. On the right panels, we plot cuts along V_{int} at $\Phi_{ext} = 0.22\Phi_0$ (blue) and $\Phi_{ext} = \Phi_0/2$ (orange). The radiation power is here presented on a linear scale. At $\Phi_{ext} = \Phi_0/2$, the $4e$ peak emerges as the dominant feature, yet its amplitude is approximately ~ 25 times smaller compared to the amplitude of the $2e$ peak measured at $\Phi_{ext} = 0.22\Phi_0$. This is expected, since the amplitude of the power emission peak is proportional to the square of I_c , which at $\Phi_{ext} = \Phi_0/2$ is only determined by the second harmonic of the CPR, and is ~ 5 times smaller than I_c at $\Phi_{ext} = 0.22\Phi_0$. A detailed analysis of the ratio

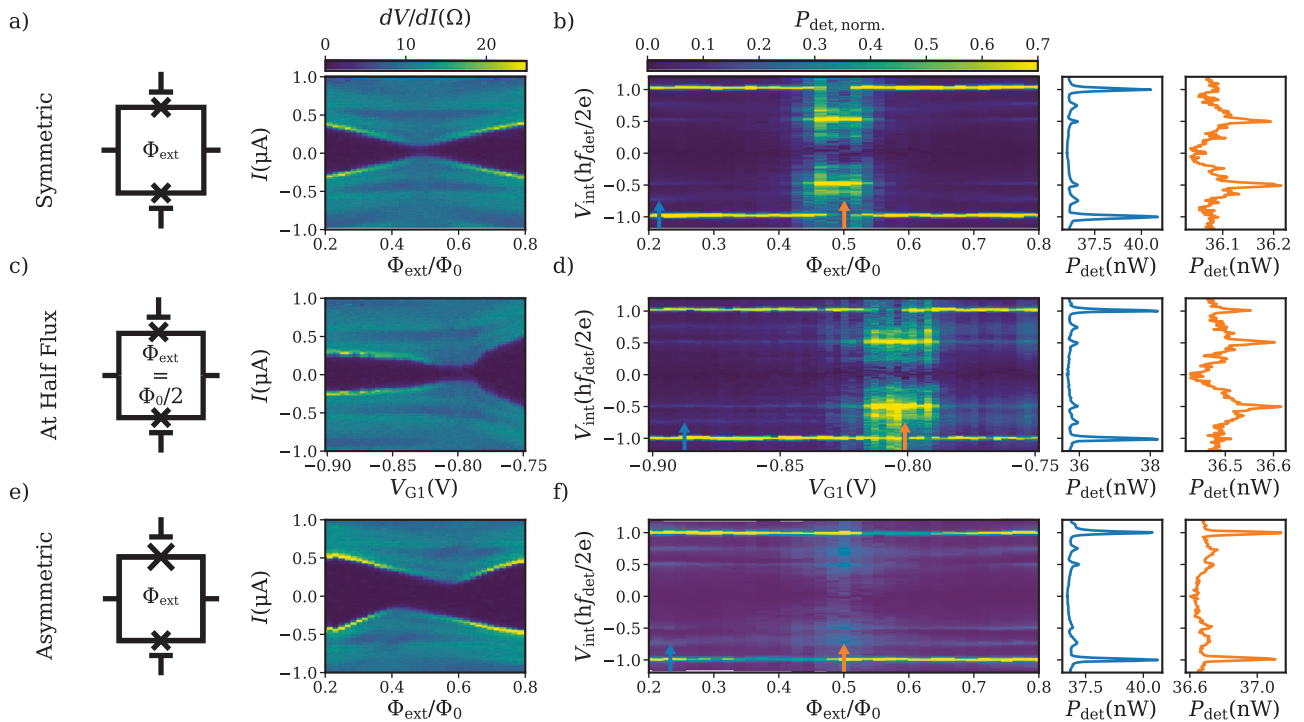


Fig. 3 Tuning a superconducting quantum interference device into a symmetric configuration. **a** Differential resistance dV/dI of the superconducting quantum interference device (SQUID) as a function of external flux Φ_{ext} and current bias I for symmetric junctions. Here, the gate voltage on one junction is $V_{G1} = -0.865$ V and the gate voltage on the other junction is $V_{G2} = -0.9$ V. In this balanced configuration, there is no diode effect. **b** Normalized radiation power $P_{\text{det, norm.}}$ at a detection frequency $f_{\text{det}} = 7.1$ GHz plotted vs external flux Φ_{ext} and normalized voltage drop over the SQUID V_{int} . The map is measured at the same time as in **a**. At half flux quantum, the $2e$ radiation signal is suppressed, and the $4e$ peak becomes the dominant feature. The plots in blue and orange are line cuts in the power map taken at $\Phi_{\text{ext}} = 0.22 \Phi_0$ and $\Phi_{\text{ext}} = \Phi_0/2$ respectively, as indicated by the arrows. In **c**, we bias the SQUID at $\Phi_{\text{ext}} = \Phi_0/2$, and fix $V_{G2} = -0.875$ V. We measure the SQUID differential resistance as a function of current bias and V_{G1} . Moving from left to right, we go from $I_{c2} > I_{c1}$ to $I_{c1} > I_{c2}$, crossing a balanced configuration. **d** Same as in **b** but for the gate and flux configuration as in **c**. For specific values of V_{G1} , we see a clear increase in the visibility of the $4e$ peak. The plots in blue and orange are line cuts in the power map taken at $V_{G1} = -0.89$ V and $V_{G1} = -0.8$ V, respectively. **e** Same as in **a**), but for $V_{G1} = -0.9$ V and $V_{G2} = -1$ V. In this unbalanced configuration, there is a diode effect. **f** Same as in **b** but for the gate configuration as in **e**. Here, throughout the flux bias range, the $2e$ peak remains the dominant feature.

between the $4e$ and $2e$ peaks can be found in Supplementary Discussion 1.

We investigate the dependence of the emission spectrum as a function of V_{G1} , when the magnetic flux is set to $\Phi_{\text{ext}} = \Phi_0/2$ and $V_{G2} = -0.875$ V, shown in Fig. 3c, d. Away from the balanced configuration, the more distinct peak in the emission spectrum is the one corresponding to the $2e$ transport. However, once we approach the balanced situation at $V_{G1} \sim -0.8$ V the signal at $V_1 = hf_{\text{det}}/2e$ is suppressed, and instead, the dominant peak in the emission spectrum becomes the one at $V_2 = hf_{\text{det}}/4e$.

Lastly, in Fig. 3e we plot the dV/dI of the SQUID as a function of I and Φ_{ext} in a gate configuration where $I_{c1} \neq I_{c2}$. Apart from $\Phi_{\text{ext}} = \Phi_0/2$, there is a clearly visible diode effect. Figure 3f shows $P_{\text{det, norm.}}$ as a function of Φ_{ext} in the same gate configuration. The $2e$ emission peak remains the dominant feature throughout the whole flux bias range. Its amplitude decreases asymmetrically on the left- and right-hand side of $\Phi_{\text{ext}} = \Phi_0/2$, following the asymmetry of the SQUID critical current. Even though the junctions are not balanced, one can still see that the emission signal slightly increases at voltages $V_2 = hf_{\text{det}}/4e$, in the vicinity of $\Phi_{\text{ext}} = \Phi_0/2$. A study of the evolution of the $4e$ peak emission amplitude at different gate voltage configurations is presented in Supplementary Discussion 2.

These findings show that a continuous transition between a $2e$ and a $4e$ supercurrent can be achieved by tuning both gate voltages and the magnetic flux. Importantly, the $4e$ supercurrent dominates over a finite window in parameter space and is not limited to exactly matching boundary conditions.

Shapiro steps. So far, we have used the Josephson radiation measurements to identify the emergence of a $4e$ supercurrent in the SQUID. In the last part of this work, we discuss Shapiro step measurements that complement the radiation experiment. When a microwave drive tone is sent to a JJ, distinct voltage plateaus in the $V(I)$ characteristic appear, known as Shapiro steps^{47–51}. For a conventional $\sin(\varphi)$ junction, each plateau corresponds to a Cooper-pair absorbing n photons with frequency f_d to overcome the Shapiro step voltage V_n , and the energy relation reads $2eV_n = nhf_d$. The presence of higher harmonics in the CPR of the junction changes the energy relation to $2meV_n = nhf_d$, corresponding to m Cooper-pairs absorbing n photons to overcome the voltage step.

We apply a microwave tone of fixed frequency $f_d = 7.5$ GHz to the SQUID with different output power P_d values. The signal is applied to the microwave input line, connecting the device to the amplification chain through a directional coupler (see Supplementary Note 1). In Fig. 4a, we plot the SQUID differential resistance dV/dI at $\Phi_{\text{ext}} = 0$ as a function of current bias I and P_d in a symmetric gate configuration. In the left panel, we plot dV/dI versus I , and on the right, we plot the data as a function of the integrated voltage V_{int} scaled by $hf_d/2e$. Shapiro steps occur at integer values of the scaled voltage as dips in differential resistance.

The data in Fig. 4b is measured for the same gate values as in Fig. 4a, but at $\Phi_{\text{ext}} = \Phi_0/2$. In this configuration, the SQUID resembles an effective $\sin(2\varphi)$ junction because the $2e$

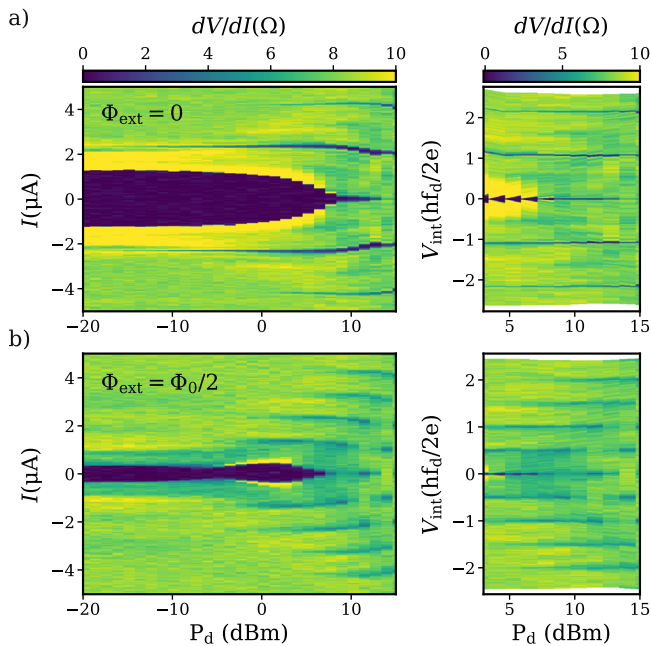


Fig. 4 Shapiro steps measurements at zero and a half flux quantum for symmetric junctions. **a** On the left, differential resistance dV/dI as a function of drive power P_d and bias current I at constant drive frequency $f_d = 7.5$ GHz and zero external flux $\Phi_{\text{ext}} = 0$ for a gate voltage on the first junction of $V_{G1} = -0.73$ V and a gate voltage on the second junction of $V_{G2} = -0.5$ V. The drops in differential resistance correspond to the emergence of Shapiro steps. On the right, differential resistance as a function of P_d plotted vs normalized voltage drop V_{int} over the device. At zero flux, mostly integer Shapiro steps are visible. **b** Same as in **a**, but at $\Phi_{\text{ext}} = \Phi_0/2$. The destructive interference of the first harmonics produces a current-phase relation with double the periodicity of the individual junctions, inducing the emergence of half-integer Shapiro steps.

supercurrent is suppressed. The energy relation for the appearance of Shapiro steps is given in this case by $4eV_n = nhf_d$, resulting in a doubling of the number of observed steps. In line with the theoretical expectations⁴⁵, both integer and half-integer Shapiro steps are equally visible in the data. Differences between this measurement and Shapiro steps measurements performed on Josephson junction with a high-quality factor⁵² are attributed to the 10 Ω -shunt in our device.

Conclusion

We have demonstrated the realization of an effective $\sin(2\varphi)$ Josephson junction using a dc SQUID consisting of two planar Josephson junctions formed in a proximitized InAs two-dimensional electron gas. We probe the emergence of a dominant second harmonic in the CPR of the SQUID by measuring the ac Josephson effect as a function of gate voltages and magnetic flux. Photon emission at the fundamental Josephson frequency is suppressed when the SQUID is in a symmetric configuration and biased at half flux and instead, photons are only emitted at $f_{J,2}$. We provide evidence on how to continuously tune from the 2e to the 4e supercurrent regime by adjusting the junction gate voltages and the external magnetic flux. The results are further substantiated through complementary Shapiro step measurements in a symmetric SQUID configuration at half flux, revealing additional half-integer steps with the same visibility as the integer steps.

Our results indicate, that a robust $\sin(2\varphi)$ JJ can be engineered and could be used to realize parity-protected qubits with this material system. Such parity-protected qubit provides an alternative route to the protection of quantum information in

superconducting devices and may complement alternative approaches based on fluxonium qubits^{53–56} and qubits based on topological wavefunctions^{57–63}. Looking ahead, the 2D platform would make it easier to further protect the qubit from noise and offsets by concatenating several SQUIDs in parallel²¹.

Methods

The proximitized InAs two-dimensional electron gas used in this project is grown starting from a semi-insulating InP (100) substrate. A 1 μm thick $\text{In}_x\text{Al}_{1-x}\text{As}$ buffer layer is used to match the lattice constant of InP to the one of InAs. The quantum well consists of a 7 nm InAs layer sandwiched between a 10 nm (top barrier) and a 4 nm (bottom barrier) $\text{In}_{0.75}\text{Ga}_{0.25}\text{As}$ layer. The 10 nm Al layer is epitaxially grown on top of a capping GaAs thin film without breaking the vacuum, ensuring a pristine interface between the semiconductor and the superconductor. Here we show results obtained from a wafer stack with mobility $\mu = 11,000$ $\text{cm}^2 \text{V}^{-1} \text{s}^{-1}$ at electron densities of $2.0 \times 10^{12} \text{cm}^{-2}$, measured on a different chip coming from the same wafer.

The device is fabricated using standard electron beam lithography techniques. The SQUID is electrically isolated by etching the Al layer and 300 nm of buffer around it. First, the Al film is removed with Al etchant Transene D, followed by a deep III-V chemical wet etch $\text{H}_2\text{O}:\text{C}_6\text{H}_8\text{O}_7:\text{H}_3\text{PO}_4:\text{H}_2\text{O}_2$ (220:55:3:3). Next, JJs are formed by selectively removing the Al over 150nm-long stripes on each branch of the loop. A 15 nm-thick layer of insulating HfO_2 is grown by atomic layer deposition at a temperature of 90 $^\circ\text{C}$ over the entire sample. The set of gates is realized in two steps. A thin Ti/Au (5/25 nm) layer is evaporated on top of the mesa to define the gate geometry, and then leads and bonding pads are defined by evaporating a Ti/Au (5/85 nm) layer at an angle of $\pm 17^\circ$ to overcome the mesa step. More information about the full wafer stack and the fabrication procedure can be found in refs. ^{31,33,34,64}.

Data availability

All data in this publication is available in numerical form at <https://doi.org/10.5281/zenodo.7969736>, ref. ⁶⁵.

Received: 20 September 2023; Accepted: 9 January 2024;

Published online: 22 January 2024

References

1. Wallraff, A. et al. Strong coupling of a single photon to a superconducting qubit using circuit quantum electrodynamics. *Nature* **431**, 162 (2004).
2. Arute, F. et al. Quantum supremacy using a programmable superconducting processor. *Nature* **574**, 505 (2019).
3. Clarke, J. & Wilhelm, F. K. Superconducting quantum bits. *Nature* **453**, 1031 (2008).
4. Castellanos-Beltran, M. A. & Lehnert, K. W. Widely tunable parametric amplifier based on a superconducting quantum interference device array resonator. *Appl. Phys. Lett.* **91** <https://doi.org/10.1063/1.2773988> (2017).
5. Krinner, S. et al. Realizing repeated quantum error correction in a distance-three surface code. *Nature* **605**, 669 (2022).
6. Frattini, N. E. et al. 3-wave mixing Josephson dipole element. *Appl. Phys. Lett.* **110**, 222603 (2017).
7. Frattini, N. E., Sivak, V. V., Lingenfelter, A., Shankar, S. & Devoret, M. H. Optimizing the nonlinearity and dissipation of a snail parametric amplifier for dynamic range. *Phys. Rev. Appl.* **10**, 054020 (2018).
8. Miano, A. et al. Frequency-tunable Kerr-free three-wave mixing with a gradiometric SNAIL. *Appl. Phys. Lett.* **120**, 184002 (2022).
9. Golubov, A. A., Kupriyanov, M. Y. & Il'ichev, E. The current-phase relation in Josephson junctions. *Rev. Mod. Phys.* **76**, 411 (2004).
10. Josephson, B. Possible new effects in superconductive tunnelling. *Phys. Lett.* **1**, 251 (1962).
11. Della Rocca, M. L. et al. Measurement of the current-phase relation of superconducting atomic contacts. *Phys. Rev. Lett.* **99**, 127005 (2007).
12. Spanton, E. M. et al. Current-phase relations of few-mode inas nanowire Josephson junctions. *Nat. Phys.* **13**, 1177 (2017).

13. Nichele, F. et al. Relating andreev bound states and supercurrents in hybrid Josephson junctions. *Phys. Rev. Lett.* **124**, 226801 (2020).
14. Endres, M. et al. Current-phase relation of a WTe₂ Josephson junction. *Nano Lett.* **23**, 4654 (2023).
15. Stoutimore, M. J. A. et al. Second-harmonic current-phase relation in Josephson junctions with ferromagnetic barriers. *Phys. Rev. Lett.* **121**, 177702 (2018).
16. Ioffe, L. B. & Feigel'man, M. V. Possible realization of an ideal quantum computer in Josephson junction array. *Phys. Rev. B* **66**, 224503 (2002).
17. Douçot, B. & Vidal, J. Pairing of cooper pairs in a fully frustrated Josephson-junction chain. *Phys. Rev. Lett.* **88**, 227005 (2002).
18. Brooks, P., Kitaev, A. & Preskill, J. Protected gates for superconducting qubits. *Phys. Rev. A* **87**, 052306 (2013).
19. Groszkowski, P. et al. Coherence properties of the 0- π qubit. *N. J. Phys.* **20**, 043053 (2018).
20. Paolo, A. D., Grimsmo, A. L., Groszkowski, P., Koch, J. & Blais, A. Control and coherence time enhancement of the 0- π qubit. *N. J. Phys.* **21**, 043002 (2019).
21. Schrade, C., Marcus, C. M. & Gyenis, A. Protected hybrid superconducting qubit in an array of gate-tunable Josephson interferometers. *PRX Quant.* **3**, 030303 (2022).
22. Smith, W. C., Kou, A., Xiao, X., Vool, U. & Devoret, M. H. Superconducting circuit protected by two-cooper-pair tunneling. *npj Quant. Inf.* **6**, 8 (2020).
23. Maiani, A., Kjaergaard, M. & Schrade, C. Entangling transmons with low-frequency protected superconducting qubits. *PRX Quantum* **3**, 030329 (2022).
24. Leroux, C. & Blais, A. Cat-qubit-inspired gate on $\cos(2\theta)$ qubits. <https://arxiv.org/abs/2304.02155> (2023).
25. Gladchenko, S. et al. Superconducting nanocircuits for topologically protected qubits. *Nat. Phys.* **5**, 48 (2009).
26. Bell, M. T., Paramanandam, J., Ioffe, L. B. & Gershenson, M. E. Protected Josephson rhombus chains. *Phys. Rev. Lett.* **112**, 167001 (2014).
27. Pop, I. M. et al. Measurement of the current-phase relation in Josephson junction rhombi chains. *Phys. Rev. B* **78**, 104504 (2008).
28. Heikkilä, T. T., Särkkä, J. & Wilhelm, F. K. Supercurrent-carrying density of states in diffusive mesoscopic Josephson weak links. *Phys. Rev. B* **66**, 184513 (2002).
29. Chauvin, M. et al. Superconducting atomic contacts under microwave irradiation. *Phys. Rev. Lett.* **97**, 067006 (2006).
30. Larsen, T. W. et al. Parity-protected superconductor-semiconductor qubit. *Phys. Rev. Lett.* **125**, 056801 (2020).
31. Kjaergaard, M. et al. Quantized conductance doubling and hard gap in a two-dimensional semiconductor-superconductor heterostructure. *Nat. Commun.* **7**, 12841 (2016).
32. Hendrickx, N. W. et al. Gate-controlled quantum dots and superconductivity in planar germanium. *Nat. Commun.* **9**, 2835 (2018).
33. Shabani, J. et al. Two-dimensional epitaxial superconductor-semiconductor heterostructures: A platform for topological superconducting networks. *Phys. Rev. B* **93**, 155402 (2016).
34. Lee, J. S. et al. Transport studies of Epi-Al/InAs two-dimensional electron gas systems for required building-blocks in topological superconductor networks. *Nano Lett.* **19**, 3083 (2019).
35. Casparis, L. et al. Superconducting gatemon qubit based on a proximitized two-dimensional electron gas. *Nat. Nanotechnol.* **13**, 915 (2018).
36. Kulik, I. O. & Omel'yanchuk, A. N. Contribution to the microscopic theory of the Josephson effect in superconducting bridges. *JETP Lett.* **21**, 216 (1975).
37. Dorokhov, O. On the coexistence of localized and extended electronic states in the metallic phase. *Solid State Commun.* **51**, 381 (1984).
38. Nazarov, Y. V. Limits of universality in disordered conductors. *Phys. Rev. Lett.* **73**, 134 (1994).
39. Beenakker, C. W. J. Random-matrix theory of quantum transport. *Rev. Mod. Phys.* **69**, 731 (1997).
40. Ciaccia, C. et al. Gate-tunable Josephson diode in proximitized InAs supercurrent interferometers. *Phys. Rev. Res.* **5**, 033131 (2023).
41. Basset, J. et al. Nonadiabatic dynamics in strongly driven diffusive Josephson junctions. *Phys. Rev. Res.* **1**, 032009 (2019).
42. Haller, R. et al. ac Josephson effect in a gate-tunable cd₃as₂ nanowire superconducting weak link. *Phys. Rev. B* **108**, 094514 (2023).
43. Haller, R. *Probing the Microwave Response of Novel Josephson Elements*. Ph.D. thesis, University of Basel, Basel (2021).
44. Jebari, S. et al. Near-quantum-limited amplification from inelastic cooper-pair tunnelling. *Nat. Electron.* **1**, 223 (2018).
45. Souto, R. S., Leijnse, M. & Schrade, C. Josephson diode effect in supercurrent interferometers. *Phys. Rev. Lett.* **129**, 267702 (2022).
46. Haxell, D. Z. et al. Measurements of phase dynamics in planar Josephson junctions and squids. *Phys. Rev. Lett.* **130**, 087002 (2023).
47. Shapiro, S., Janus, A. R. & Holly, S. Effect of microwaves on Josephson currents in superconducting tunneling. *Rev. Mod. Phys.* **36**, 223 (1964).
48. Raes, B. et al. Fractional Shapiro steps in resistively shunted Josephson junctions as a fingerprint of a skewed current-phase relationship. *Phys. Rev. B* **102**, 054507 (2020).
49. Ueda, K. et al. Evidence of half-integer Shapiro steps originated from nonsinusoidal current phase relation in a short ballistic InAs nanowire Josephson junction. *Phys. Rev. Res.* **2**, 033435 (2020).
50. Iorio, A. et al. Half-integer Shapiro steps in highly transmissive InSb nanoflag Josephson junctions. *Phys. Rev. Res.* **5**, 033015 (2023).
51. Valentini, M. et al. Radio frequency driven superconducting diode and parity conserving cooper pair transport in a two-dimensional germanium hole gas. <https://arxiv.org/abs/2306.07109> (2023).
52. Le Calvez, K. et al. Joule overheating poisons the fractional ac Josephson effect in topological Josephson junctions. *Commun. Phys.* **2**, 4 (2019).
53. Manucharyan, V. E., Koch, J., Glazman, L. I. & Devoret, M. H. Fluxonium: Single cooper-pair circuit free of charge offsets. *Science* **326**, 113 (2009).
54. Nguyen, L. B. et al. High-coherence fluxonium qubit. *Phys. Rev. X* **9**, 041041 (2019).
55. Hazard, T. M. et al. Nanowire superinductance fluxonium qubit. *Phys. Rev. Lett.* **122**, 010504 (2019).
56. Somoroff, A. et al. Millisecond coherence in a superconducting qubit. <https://arxiv.org/abs/2103.08578> (2021).
57. Hoffman, S., Schrade, C., Klinovaja, J. & Loss, D. Universal quantum computation with hybrid spin-majorana qubits. *Phys. Rev. B* **94**, 045316 (2016).
58. Rančić, M. J., Hoffman, S., Schrade, C., Klinovaja, J. & Loss, D. Entangling spins in double quantum dots and majorana bound states. *Phys. Rev. B* **99**, 165306 (2019).
59. Schrade, C. & Fu, L. Majorana superconducting qubit. *Phys. Rev. Lett.* **121**, 267002 (2018).
60. Schrade, C. & Fu, L. Quantum computing with Majorana Kramers pairs. *Phys. Rev. Lett.* **129**, 227002 (2022).
61. Landau, L. A. et al. Towards realistic implementations of a Majorana surface code. *Phys. Rev. Lett.* **116**, 050501 (2016).
62. Plugge, S., Rasmussen, A., Egger, R. & Flensberg, K. Majorana box qubits. *N. J. Phys.* **19**, 012001 (2017).
63. Karzig, T. et al. Scalable designs for quasiparticle-poisoning-protected topological quantum computation with majorana zero modes. *Phys. Rev. B* **95**, 235305 (2017).
64. Shabani, J., Das Sarma, S. & Palmstrøm, C. J. An apparent metal-insulator transition in high-mobility two-dimensional InAs heterostructures. *Phys. Rev. B* **90**, 161303 (2014).
65. Ciaccia, C. Data for "Charge-4e supercurrent in an InAs-Al superconductor-semiconductor heterostructure" <https://arxiv.org/abs/2306.05467> (2023).

Acknowledgements

We thank C. M. Marcus for his support in initiating this work and collaboration. We thank Libin Wang for his help in the development of the fabrication procedure. We thank Joost Ridderbos and Gergő Fülöp for their help with the setup and the understanding of the measurements in the early stage of the experiment. We thank Martin Endres for the fruitful discussions. This research was supported by the Swiss Nanoscience Institute (SNI), the Swiss National Science Foundation through grants Nos. 172638 and 192027, and the QuantEra project SuperTop. We further acknowledge funding from the European Union's Horizon 2020 research and innovation program, specifically (a) from the European Research Council (ERC) grant agreement No. 787414, ERC-Adv TopSupra, (b) grant agreement No. 828948, FET-open project AndQC, and (c) grant agreement 847471, project COFUND-QUSTEC. Constantin Schrade acknowledges support from the Microsoft Corporation.

Author contributions

C.C. fabricated the device and performed the measurements with the help of R.H. C.C. and R.H. analyzed the data with inputs from A.C.C.D. and Constantin Schrade. C.C. wrote the manuscript with inputs from all authors. Christian Schönenberger initiated the project. T.L. and M.M. provided the InAs material.

Competing interests

The authors declare no competing interests.

Additional information

Supplementary information The online version contains supplementary material available at <https://doi.org/10.1038/s42005-024-01531-x>.

Correspondence and requests for materials should be addressed to Carlo Ciaccia.

Peer review information *Communications Physics* thanks Peng Yu and the other, anonymous, reviewer(s) for their contribution to the peer review of this work.

Reprints and permission information is available at <http://www.nature.com/reprints>

Publisher's note Springer Nature remains neutral with regard to jurisdictional claims in published maps and institutional affiliations.



Open Access This article is licensed under a Creative Commons Attribution 4.0 International License, which permits use, sharing, adaptation, distribution and reproduction in any medium or format, as long as you give appropriate credit to the original author(s) and the source, provide a link to the Creative Commons license, and indicate if changes were made. The images or other third party material in this article are included in the article's Creative Commons license, unless indicated otherwise in a credit line to the material. If material is not included in the article's Creative Commons license and your intended use is not permitted by statutory regulation or exceeds the permitted use, you will need to obtain permission directly from the copyright holder. To view a copy of this license, visit <http://creativecommons.org/licenses/by/4.0/>.

© The Author(s) 2024